Mon. Not. R. Astron. Soc. **262,** 855–867 (1993)

The combined effect of partial redistribution and non-coherent electron scattering on polarized resonance line transfer

K. N. Nagendra, K. E. Rangarajan and D. Mohan Rao
Indian Institute of Astrophysics, Bangalore 560 034, India

Accepted 1992 December 4. Received 1992 November 30; in original form 1992 August 5

ABSTRACT

The combined effect of partial frequency redistribution by atoms (PRD) and non-coherent electron scattering (NCES) on line formation is studied, taking account of the polarization state of the radiation field in resonance line scattering. For the purpose of comparison, a study is also made of redistribution by other mechanisms, namely complete redistribution (CRD) and coherent scattering (CS) combined with NCES. A static medium stratified into plane-parallel homogeneous layers is considered. A conventional two-level atom approximation is employed as the basic model. The emergent linear polarization profile exhibits interesting characteristics in its variation across the line profile. Atomic redistribution plays an important role at the line core and the near wings of the resonance line. Electron scattering, however, makes significant contributions in the far wings ($x > 10$). For resonance lines with high optical thickness, NCES leads to measurable changes of polarization in the far wings irrespective of the atomic scattering mechanism employed. Since electron scattering is a dominant source of the scattering of continuum and line photons in hot stars, and particularly in supernova atmospheres, it is important to include the non-coherent electron scattering mechanism correctly when computing emergent intensity and polarization profiles for these objects.

Key words: atomic processes – line: formation – polarization – radiative transfer – scattering.

1 INTRODUCTION

The importance of electron scattering in stellar line formation problems has been recognized for a long time. Detailed reference to earlier work in this field is made by Rangarajan, Mohan Rao & Peraiah (1991). Several years ago, Auer & Mihalas (1968) considered the problem of line transfer employing non-coherent 'isotropic' electron scattering and complete redistribution (CRD) in a two-level atom model with a Doppler profile function. Rangarajan et al. (1991) have solved a more general problem involving atomic partial redistribution (PRD) and non-coherent isotropic electron scattering (NCES). Recently, Hillier (1991) has considered the effect of electron scattering on line profiles formed in the expanding atmospheres of early-type stars. He employed a comoving frame method as well as a Monte Carlo method to solve the radiative transfer problem, including non-coherent electron redistribution combined with atomic complete redistribution. In a series of papers, Hillier (1991, and references therein to earlier papers) demonstrated the need for correct consideration of electron scattering in the derivation of correct mass-loss rates in O and B stars. He also pointed out the discrepancy caused by neglect of the electron scattering in the line wings of diagnostic line profiles. It is well known that line wing polarization of supernova line profiles can be used to probe the asymmetry of the electron-scattering atmospheres of supernovae and to derive the electron density distribution in the atmospheric layers. In this paper, we confine our attention to theoretical aspects of line formation, including the polarization state of radiation, when the scattering is 'anisotropic' and non-coherent, on atoms in a two-level atom model as well as on free electrons. In Section 2 we describe the relevant equations. In Section 3 the results of the computations are presented and discussed in detail. Finally, in Section 4 our conclusions are given.

2 THE POLARIZED LINE TRANSFER EQUATION AND THE METHOD OF SOLUTION

If the radiation field is azimuthally symmetric, consideration of the Stokes parameters I_ℓ and I_r is sufficient to represent completely the polarization state of the radiation field in a plane-parallel (PP) medium. The scalar total intensity is defined as $I = I_\ell + I_r$, the Stokes Q parameter is defined as $Q = I_\ell - I_r$ and the percentage of linear polarization is defined as $p = (Q/I) \times 100$. The vector transfer equation for the two-component vector $\mathbf{I} = (I_\ell \; I_r)^T$ is given by

$$\mu \frac{d\mathbf{I}(x, \mu, z)}{dz} = -\chi(x, \mu, z)\, \mathbf{I}(x, \mu, z) + \boldsymbol{\eta}(x, \mu, z), \tag{1}$$

in the conventional notation of two-level atom line transfer problems. The total absorption coefficient is given by

$$\chi(x, \mu, z) = \chi^L(z)\, \phi(x, \mu, z) + \chi^C(x, \mu, z) + \chi^e(x, \mu, z), \tag{2}$$

and the optical depth scale is defined as $d\tau(z) = -\chi^L(z)\, dz$, where the reduced frequency x is defined as

$$x = \frac{\nu - \nu_0}{\Delta\nu_D}, \tag{3}$$

with

$$\Delta\nu_D = \frac{\nu_0}{c}\sqrt{\frac{2kT}{M^a}}.$$

In equation (2), χ^C and χ^e are the coefficients of continuous absorption and electron scattering ($\chi^e = N_e \sigma_e$, where σ_e is the Thomson scattering coefficient and N_e the electron number density) respectively, and χ^L is the line-averaged atomic absorption coefficient at the line centre. The profile function is represented by a Voigt function:

$$\phi(x) = \frac{1}{\sqrt{\pi}} H(a, x), \tag{4}$$

where the Voigt parameter a represents a constant ratio of the damping width to the Doppler width. The emission coefficient is analogously defined as

$$\boldsymbol{\eta}(x, \mu, z) = \boldsymbol{\eta}^L(x, \mu, z) + \boldsymbol{\eta}^C(x, \mu, z) + \boldsymbol{\eta}^e(x, \mu, z), \tag{5}$$

with the superscripts L, C and e indicating line, continuum and electrons respectively. The total source function $\mathbf{S}_{tot}(x, \mu, z)$ is given by

$$\mathbf{S}_{tot}(x, \mu, z) = \frac{\boldsymbol{\eta}(x, \mu, z)}{\chi(x, \mu, z)} = \frac{\mathbf{S}^L(x, \mu, z)\, \phi(x) + \mathbf{S}^C(\chi^C/\chi^L) + \mathbf{S}^e(x, \mu, z)\, (\chi^e/\chi^L)}{\phi(x) + (\chi^C/\chi^L) + (\chi^e/\chi^L)}. \tag{6}$$

Notice that, in equation (6) above, we have retained with physical variables only those arguments inside the brackets that pertain to the models presented in this paper, namely the isothermal, the constant-property and the static-atmosphere models. It is straightforward, however, to consider the dependence of these variables on all the physical and geometric parameters. Defining the continuum atomic absorption parameter as $\beta_C = (\chi^C/\chi^L)$, and the continuum electron-scattering parameter as $\beta_e = (\chi^e/\chi^L)$, we can rewrite equation (6) as

$$\mathbf{S}_{tot}(x, \mu, z) = \frac{\phi(x)\, \mathbf{S}^L(x, \mu, z) + \beta_C \mathbf{S}^C + \beta_e \mathbf{S}^e(x, \mu, z)}{\phi(x) + \beta_C + \beta_e}, \tag{7}$$

where the continuum source function $\mathbf{S}^C$ is defined as

$$\mathbf{S}^C = \frac{1}{2} B(x)\, \mathbf{1} = \frac{1}{2} B\mathbf{1}; \qquad \mathbf{1} = (1 \quad 1)^T, \tag{8}$$

where the continuum absorption parameter β_C is assumed to be frequency-independent across the entire bandwidth of the line. A two-level atom line source vector is given by

$$\mathbf{S}^L(x, \mu, z) = \begin{bmatrix} S_\ell^L(x, \mu, z) \\ S_r^L(x, \mu, z) \end{bmatrix} = \frac{(1-\varepsilon)}{\phi(x)} \int_{-\infty}^{+\infty} dx' \int_{-1}^{+1} \mathbf{R}^a(x, \mu, x', \mu')\, \mathbf{I}(x', \mu', z)\, d\mu' + \frac{\varepsilon}{2} B\mathbf{1}, \tag{9}$$

where ε is the probability per scatter that a photon is destroyed by collisional de-excitation. The redistribution matrix $\mathbf{R}^{\mathrm{a}}(x, \mu, x', \mu')$ accounts for the correlations in frequency, angle and polarization state that exist between the incident photon, characterized by (x, μ), and the re-emitted photon, characterized by (x', μ'), during a scattering event involving a two-level atom, and incident and re-emitted photons. This matrix can be approximated for scattering on a two-level atom, in the form

$$\mathbf{R}^{\mathrm{a}}(x, \mu, x', \mu') = \mathbf{P}^{\mathrm{a}}(\mu, \mu')\, R^{\mathrm{a}}(x, x'), \tag{10}$$

where the angular phase matrix for resonance scattering is defined as

$$\mathbf{P}^{\mathrm{a}}(\mu, \mu') = \frac{3}{8} E_1 \begin{bmatrix} 2(1-\mu^2)(1-\mu'^2)+\mu^2\mu'^2 & \mu^2 \\ \mu'^2 & 1 \end{bmatrix} + \frac{(1-E_1)}{4} \begin{pmatrix} 1 & 1 \\ 1 & 1 \end{pmatrix}, \tag{11}$$

where $(1 - E_1)$ measures the amount of atomic depolarization. E_1 depends on the angular momentum quantum numbers, j_ℓ and j_{u}, of the transition involved (ℓ = lower state, u = upper state). Maximum polarization occurs for the $(j_\ell = 0) \rightarrow (j_{\mathrm{u}} = 1)$ type of transition, when $E_1 = 1$. In this special case, $\mathbf{P}^{\mathrm{a}}(\mu, \mu')$ reduces to the classical Rayleigh scattering phase matrix (see Chandrasekhar 1950 for details). The quantity $R^{\mathrm{a}}(x, x')$ in equation (10) is the conventional scalar redistribution function. A good discussion of the frequency and angle separation implied in equation (10) is given by Faurobert (1987). The following atomic redistribution functions, in Hummer's notation, are used in this paper:

CS: $$R^{\mathrm{a}}(x, x') = \delta(x - x')\, \phi(x'), \tag{12}$$

CRD: $$R^{\mathrm{a}}(x, x') = \phi(x)\, \phi(x'), \tag{13}$$

PRD: $$R^{\mathrm{a}}(x, x') = R^{\mathrm{a}}_{\mathrm{II-A}}(x, x'), \tag{14}$$

with

$$R^{\mathrm{a}}_{\mathrm{II-A}}(x, x') = \pi^{-3/2} \int_{1/2|\bar{x}-\underline{x}|}^{\infty} \mathrm{e}^{-u^2} \left[\tan^{-1}\left(\frac{\underline{x}+u}{a}\right) - \tan^{-1}\left(\frac{\bar{x}-u}{a}\right) \right] \mathrm{d}u, \tag{15}$$

where $\bar{x}$ denotes $\max(x, x')$ and $\underline{x}$ denotes $\min(x, x')$ and the redistribution function $R^{\mathrm{a}}_{\mathrm{II-A}}(x, x')$ is the well-known type II − A redistribution function of Hummer (1962), which is an angle-averaged scalar redistribution function for isotropic scattering. It refers to a case of a two-level atom whose upper level is naturally broadened and whose lower level has zero width. Analogously to equation (9), the electron-scattering source function $\mathbf{S}^{\mathrm{e}}(x, \mu, z)$ is given by

$$\mathbf{S}^{\mathrm{e}}(x, \mu, z) = \begin{bmatrix} S^{\mathrm{e}}_{\ell}(x, \mu, z) \\ S^{\mathrm{e}}_{\mathrm{r}}(x, \mu, z) \end{bmatrix} = \int_{-\infty}^{+\infty} \mathrm{d}x' \int_{-1}^{+1} \mathbf{R}^{\mathrm{e}}(x, \mu, x', \mu')\, \mathbf{I}(x', \mu', z)\, \mathrm{d}\mu', \tag{16}$$

where β_{e} is the ratio of the electron-scattering coefficient to the line-centre absorption coefficient, defined above. Expressions for the non-coherent electron redistribution matrix and the angular phase matrix can be obtained by equations (10) and (11), through a replacement of superscript a by e, and by taking $E_1 = 1$. The angle-independent redistribution function for electron scattering can be selected from the following types:

CES: $$R^{\mathrm{e}}(x, x') = \delta(x - x'), \tag{17}$$

NCES: $$R^{\mathrm{e}}(x, x') = R^{\mathrm{e}}_{\mathrm{A}}(x, x'), \tag{18}$$

where CES refers to coherent electron scattering and $R^{\mathrm{e}}_{\mathrm{A}}(x, x')$ is the angle-averaged non-coherent electron redistribution function given by

$$R^{\mathrm{e}}_{\mathrm{A}}(x, x') = \left(\frac{1}{\omega}\right) \mathrm{ierfc} \left| \frac{x - x'}{2\omega} \right| \tag{19}$$

(see Auer & Mihalas 1968). ω is the ratio of the electron Doppler width $\Delta\nu_{\mathrm{e}}$ to the atomic Doppler width $\Delta\nu_{\mathrm{D}}$, given by

$$\omega \simeq 43\sqrt{A}, \tag{20}$$

where A is the atomic weight of the atom under consideration. The function ierfc, which is the integral of the complimentary error function, is given explicitly as

$$\mathrm{ierfc}(z) = \int_z^{\infty} \mathrm{erfc}(x)\, \mathrm{d}x = \frac{1}{\sqrt{\pi}} \mathrm{e}^{-z^2} - z[\mathrm{erfc}(z)]. \tag{21}$$

The reduced frequency scale x_e can be defined in terms of the electron Doppler width as

$$x_e = \frac{(\nu - \nu_0)}{\Delta\nu_e},$$

with

$$x = \omega x_e.$$

Finally, the boundary conditions employed in the solution of the transfer equation, for all the models presented here, are

$$\mathbf{I}(x, \mu, \tau = T) = 0.5 \qquad \text{at } \tau = T \tag{22}$$

and

$$\mathbf{I}(x, -\mu, \tau = 0) = 0.0 \qquad \text{at } \tau = 0, \tag{23}$$

unless otherwise stated for specific models. The following expressions are useful for understanding the results presented in this paper. Starting with equation (7), the total source function for the I Stokes parameter only can be written as

$$S^I_{\rm tot}(x, \mu, z) = \frac{\phi(x)\{S(x, z) + [(1/3) - \mu^2]\, P(x, z)\} + \beta_C B + \beta_e\{S^e(x, z) + [(1/3) - \mu^2]\, P^e(x, z)\}}{\phi(x) + \beta_C + \beta_e}, \tag{24}$$

where the unpolarized atomic scalar source function is given by

$$S(x, z) = \frac{(1 - \varepsilon)}{2\phi(x)} \int_{-\infty}^{\infty} R^a(x, x')\, dx' \int_{-1}^{1} I(x', \mu', z)\, d\mu' + \varepsilon B. \tag{25}$$

The polarized part of the total source function for atomic redistribution is given by

$$P(x, z) = \frac{3(1 - \varepsilon)}{16\phi(x)} \int_{-\infty}^{\infty} R^a(x, x')\, dx' \int_{-1}^{1} [(1 - 3\mu'^2)\, I(x', \mu', z) + 3(1 - \mu'^2)\, Q(x', \mu', z)]\, d\mu' \tag{26}$$

(see Rees 1978). Corresponding expressions for non-coherent electron scattering are, respectively,

$$S^e(x, z) = \frac{1}{2} \int_{-\infty}^{\infty} R^e(x, x')\, dx' \int_{-1}^{1} I(x', \mu', z)\, d\mu' \tag{27}$$

and

$$P^e(x, z) = \frac{3}{16} \int_{-\infty}^{\infty} R^e(x, x')\, dx' \int_{-1}^{1} [(1 - 3\mu'^2)\, I(x', \mu', z) + 3(1 - \mu'^2)\, Q(x', \mu', z)]\, d\mu'. \tag{28}$$

The total source function for the Q Stokes parameter can be written as

$$S^Q_{\rm tot}(x, \mu, z) = \frac{\phi(x)(1 - \mu^2)\, P(x, z)}{\phi(x) + \beta_C + \beta_e} + \frac{(1 - \mu^2)\, P^e(x, z)}{\phi(x) + \beta_C + \beta_e}. \tag{29}$$

Notice that all the expressions given in this section represent resonance line polarization of purely atomic origin, when we set $\beta_e = 0$.

2.1 Computational details

A general discussion of the computational details is given in Rangarajan et al. (1991) and Nagendra (1988). Electron scattering makes significant contributions only in the far wings of the line profile. Thus in order to perform accurate transfer calculations it is necessary to select a very wide frequency band ($x_{\rm max} \sim 300$–400, even for a helium atom with atomic weight $A = 4$) and, therefore, a large number of frequency points in order to perform frequency integrals accurately. In practical terms, it becomes computationally very expensive to deal with this problem. In view of this difficulty, the frequency grid is split into two regions of integration, $(0, x_1)$ and (x_1, ∞), the former for dealing with atomic redistribution and the latter for dealing with electron redistribution. The total half-bandwidth selected is approximately 4 electron Doppler widths for a He atom, which corresponds

to 320 atomic Doppler widths. For frequency integrations, a 27-point frequency quadrature is employed between $x=0$ and 320. For angular integrations, a 3-point Gaussian quadrature is employed in the range $\mu\in(0, 1)$. The scattering integral over the atomic redistribution function $R^{a}_{II-A}(x, x')$ is performed by a natural cubic-spline representation of the radiation field (the algorithm due to Adams, Hummer & Rybicki 1971).

3 RESULTS AND DISCUSSION

In this section we present the results of computation using parametrized models. Each subsection pertains to the effect of an important parameter on line formation, or highlights an important aspect of line formation, illustrated with a figure. The abscissa refers to reduced frequency units on a logarithmic scale (the line centre $x=0$ is not included, but the physical quantities at $\log x=-0.3$ differ very little from those at the line centre). The ordinates refer to $\log I(x, \mu_1=0.11, \tau=0)$, and to the percentage of emergent linear polarization $p(x, \mu_1=0.11, \tau=0)$, in the upper and lower halves of the figures respectively. The basic two-level atomic model parameters remain the same for all the models, unless indicated explicitly inside the figure panel or in the corresponding figure caption. Since the profiles are symmetric with respect to the line centre, only half of the profile is shown. The standard model parameters are $\varepsilon=10^{-4}$, $\beta_C=0$, $\beta_e=0$ (or 10^{-5}), $a=2\times10^{-3}$, and $B=1$, unless stated otherwise. We illustrate our results through emergent intensity and polarization profiles only. There is therefore a need to relate them to an important macroscopic quantity that is representative of a given model, namely the optical depth dependence of the source functions S^I_{tot} and S^Q_{tot}. This can be done by employing the Eddington–Barbier relation, according to which the emergent Stokes parameters can be obtained (approximately) by

$$I(x, \mu, \tau=0)=S^I_{tot}\left(x, \mu, \tau=\frac{\mu}{\phi(x)}\right) \tag{30}$$

and

$$Q(x, \mu, \tau=0)=S^Q_{tot}\left(x, \mu, \tau=\frac{\mu}{\phi(x)}\right), \tag{31}$$

and the percentage of emergent polarization is given (approximately) by

$$p(x, \mu, \tau=0)=\frac{S^Q_{tot}\{x, \mu, \tau=\mu/[\phi(x)]\}}{S^I_{tot}\{x, \mu, \tau=\mu/[\phi(x)]\}}\times 100. \tag{32}$$

It can be seen that the term involving Stokes parameter $Q(x', \mu', z)$ which occurs on the right-hand side of equations (26) and (28) is in most of the cases small compared to the other terms. Since $S^I_{tot}[x, \mu, \tau=\mu/\phi(x)]$ in equation (32) is always positive, the sign of polarization depends on the sign of $S^Q_{tot}[x, \mu, \tau=\mu/\phi(x)]$ only. However, the sign of $S^Q_{tot}[x, \mu, \tau=\mu/\phi(x)]$ is determined by the factor $[J(x', z)-3K(x', z)]$ in equations (26) and (28), where $J(x', z)$ and $K(x', z)$ are the zeroth and second moments of specific intensity. For limb-darkened radiation, $J(x', z)<3K(x', z)$, and, for limb-brightened radiation, $J(x', z)>3K(x', z)$. Limb-darkened radiation therefore drives negative polarization and a limb-brightened radiation field gives positive polarization. Using the Eddington–Barbier relation, we can see that the major contribution to $S^Q_{tot}[x=0, \mu, \tau=\mu/\phi(x=0)]$ comes from the outermost layers, where $\tau(x)\ll 1$. The polarization at the line centre therefore directly represents the emergent intensity and the source function. Since emergent intensity is limb-darkened, we obtain negative polarization at the line centre in all cases.

3.1 Electron redistribution effects in optically thin atmospheres

In Fig. 1, we show the effect of electron scattering when the mechanisms of atomic frequency redistribution considered are CRD, PRD and CS in a constant-opacity isothermal self-emitting slab. Since in a constant-opacity isothermal slab photons travel with equal probability in all directions, it is easiest to understand the degree of linear polarization and the change of its sign across the line profile in terms mainly of the 'depth-dependent anisotropy' of the diffuse radiation field. The profiles are identified by the scattering mechanisms involved. The profiles corresponding to the case where electron scattering is neglected ($\beta_e=0$) are identified by curves 1, 2 and 3 respectively for CRD, PRD and CS. Curves 4, 5 and 6 represent, respectively, the corresponding cases when non-coherent electron scattering (NCES) is included ($\beta_e=10^{-5}$). To start with, we shall consider CRD profiles. A comparison of CRD and (CRD + NCES) profiles (curves 1 and 4) shows that the intensity at the line core or at the near-wing maxima is not affected by the inclusion of non-coherent electron scattering. Around $x=60$, the (CRD + NCES) intensity profile has an insignificant bulge compared to the pure CRD case. The corresponding polarization profile, however, shows a marked enhancement of polarization around $x=60$. Indeed, it appears that an electron-scattering polarization profile is superposed on the wing of the atomic polarization profile. From curve 4, we can see that the (CRD + NCES) polarization profile

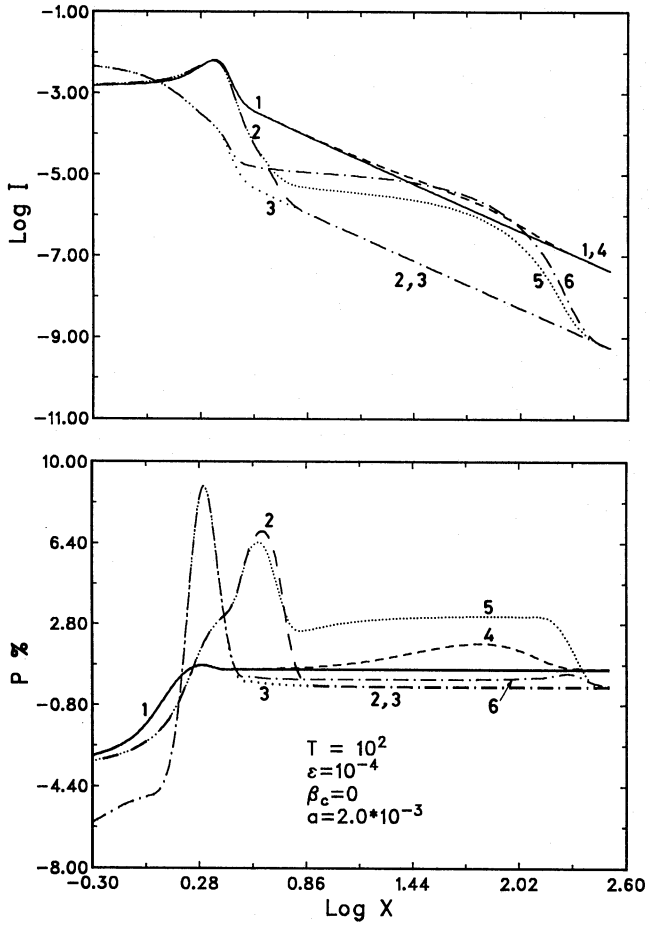

Figure 1. Emergent intensities $I(x, \mu_1)$ (upper panel) and polarizations $p(x, \mu_1)$ (lower panel) in the direction $\mu_1 = 0.11$ for the given model represented by $(T, a, \varepsilon, \beta_C, \beta_e)$. The abscissa gives the frequency x measured from the line centre in units of the Doppler width. The medium is an isothermal slab with constant physical properties. Curves 1 (solid line), 2 (long-dashed line) and 3 (widely spaced dotted line) represent the results for CRD, PRD and CS respectively, when the electron-scattering parameter $\beta_e = 0$ (i.e. no electron scattering). Curves 4 (short-dashed line), 5 (closely spaced dotted line) and 6 (dot–dashed line) represent the corresponding cases when non-coherent electron scattering (NCES) is included through the parameter $\beta_e = 10^{-5}$. The figure shows the effect of electron scattering on lines formed in an optically thin ($T = 10^2$) self-emitting slab.

has a positive, flat (frequency-independent) shape beyond $x \sim 250$. This can be seen from the polarization profile (curve 4) for $\log x > 2.4$. However, on the blue side of the maxima ($x < 60$), the CRD mechanism is stronger.

We now discuss the (PRD + NCES) results (curves 2 and 5). Here $\beta_e = 10^{-5}$, and hence the electron-scattering optical depth $T^e = \beta_e T = 10^{-3}$. Since the profile function for non-coherent electron scattering $\phi^e(x_e) = 1$, the monochromatic electron-scattering optical depth $\phi^e(x_e)\, T^e = 10^{-3}$ throughout the bandwidth considered. Clearly, $T^e \gg T^C$ in the very far wings, where $x_e \gg 1$, resulting in complete dominance of NCES in line transfer at these frequencies. The partial coherence of PRD, as represented by R^a_{II-A}, localizes photons in the far-wing frequencies, which are in turn scattered by free electrons. The electron scattering process Doppler-redistributes these photons during scattering events. Each electron scattering imparts an enormous frequency shift to the scattered photon and helps a line core photon to escape through a wing frequency. As electrons are assumed to have a Maxwellian velocity distribution, the scattered photons have a large probability of undergoing a frequency change of approximately 43 atomic Doppler widths. Thus we can interpret the intensity profile due to electron scattering in the frequency range $(40 < x < 160)$ as just a frequency mapping after a single scattering of the atomic line photons originally belonging to the range $(0 \leq x \leq 10)$. Thus NCES drains off photons in this frequency range (mainly the photons within a few Doppler widths about the line centre) into far wings (see also Rangarajan et al. 1991 and Auer & Mihalas 1968). However, when NCES is operating, near-wing ($x \simeq 2$) positive polarization peaks are slightly shifted towards the line centre and the peak values decrease. The (PRD + NCES) polarization profile (curve 5) starts deviating from the PRD profile (curve 2) around $x = 4$, and produces a characteristic positive polarization profile which remains almost frequency-independent up to $x = 160$ and then swiftly decreases to reach the polarization values of the pure PRD case. NCES produces as much as 3 per cent positive polarization in spite of a small electron optical depth. The source functions due to NCES are given by $S^e(x, z)$ and $P^e(x, z)$ (see

equations 27 and 28). The source function $S^e(x, z)$ is weakly dependent on frequency. The NCES contribution to $S^Q_{tot}(x, \mu, z)$ (see equation 29) comes from $P^e(x, z)$ only. In the wings, $\phi(x) < \beta_e$, and therefore the frequency dependences of polarization in the numerator and denominator of equation (32) are analogous and cancel out, to give a large frequency-independent polarization in the wing.

From Fig. 1, we find that CS gives a higher percentage of polarization at the line centre (~ -6 per cent) than do the PRD and CRD mechanisms (~ -3.2 per cent). CS with and without NCES (curves 3 and 6) behaves similarly, except in the far wings, where (CS + NCES) gives a small percentage of constant polarization, unlike pure CS, which produces almost negligible linear polarization. CS gives very high (9 per cent) polarization at $x \sim 2.0$. Since photons are trapped in the core for CS, they undergo a higher number of non-diffusive scatterings at the line centre than they do for CRD and PRD. Negative polarization is a consequence of multiple scattering and hence we get a higher percentage of negative polarization for CS than for CRD and PRD.

In the present case, the medium is effectively thin, $\varepsilon T \ll 1$, when $T = 10^2$. For CS, the thermalization is reached at depths smaller than those for PRD. There is therefore substantial (~ 3 per cent) polarization in the wings for PRD, unlike for the case of CS. In the CRD case, the contribution to $S^Q_{tot}(x, \mu, z)$ comes from the integral $\int \phi(x')[J(x', z) - 3K(x', z)]\,dx'$. This shows that the radiation fields, from all frequencies, determine the polarization at a given frequency. At some frequencies, $J(x', z) < 3K(x', z)$, and, at other frequency points, $J(x', z) > 3K(x', z)$. The cumulative effect is therefore to reduce the percentage of polarization in the wings (a peak value of ~ 2 per cent around $x = 40$). A contribution to the above integral comes from the slab centre, which leads to frequency-independent polarization behaviour, in general, for CRD in the wings. This point is also explained in Faurobert (1987). From the intensity profiles, we see that CRD and PRD give a self-reversal in the Doppler core, whereas CS gives emission lines. We find that NCES always gives higher intensity in the wings. This point has been explained by Rangarajan et al. (1991). PRD and CS produce lower intensity in the wings than does CRD, because photons available at the Doppler core are not allowed to diffuse into the wings by the former mechanisms.

3.2 Electron redistribution effects in moderately optically thick atmospheres

In Fig. 2, we show the effect of NCES in combination with CRD, PRD and CS when the medium is moderately optically thick ($T = 10^4$). The slab is illuminated at the bottom (at $\tau = T$). This total optical depth corresponds to a case of a moderately effectively thick ($\varepsilon T = 1$) atmosphere. It is also moderately optically thick [$(aT)^{1/3} = 2.7$] (see Hubeny 1985). Hence the emergent intensity profile $I(x, \mu_1, \tau = 0)$ is in absorption and is limb-darkened, and the polarization at the line centre is negative. There is also continuum unpolarized radiation incident on the slab, and the line wing radiation is dominated by this directly transmitted radiation which smears away any structures in the wings of the line profile. A detailed discussion of the effects of all physical parameters on the polarized absorption profiles is given in Nagendra (1988). Basically, the electron scattering causes a limb darkening in the entire line wing. Due to this, a frequency-independent emergent polarization [$p(x, \mu_1) = -0.2$ per cent] is seen. Thus, in moderately thick slabs, electron scattering produces limb darkening and negative polarization in the line wings, when CRD is the atomic line-scattering mechanism. We shall now consider the effect of NCES in combination with the partial redistribution PRD in the atomic line scattering (curves 2 and 5). The emergent polarization profile $p(x, \mu_1)$ has a second negative maximum at $x = 4$ and remains constant and negative in the wings. The effect of NCES is to produce limb darkening and increase the anisotropy of the radiation field in the wings. We next consider the profiles corresponding to the (CS + NCES) case (curves 3 and 6). Anisotropy of the radiation field [indicated by $J(x, z)/K(x, z)$] remains constant in the Doppler core for CS, and hence we obtain a constant percentage of polarization. In the wings, radiation comes from the deepest layers, where we have imposed isotropic and frequency-independent input radiation, which results in zero polarization in the wings. Electron scattering, as in the cases of CRD and PRD, produces a limb darkening and a constant and small negative polarization in the line wings. Moreover, in both the cases of CS and (CS + NCES), a small negative polarization hump appears at $x = 2.5$, such as that observed in the case of (PRD + NCES). Note also that NCES has significant opacity in the wings to prevent the intensity profiles from reaching the continuum (see intensity curves 4, 5 and 6).

3.3 Electron redistribution effects in optically thick atmospheres

Fig. 3 shows the profiles formed in a slab of optical thickness $T = 10^8$ which is irradiated at the lower boundary. This total optical depth corresponds to the case of an effectively thick ($\varepsilon T = 10^4$) and optically thick [$(aT)^{1/3} = 58.4$] slab. The NCES has a dramatic effect in this case. Basically, the impact of electron scattering is so strong ($T^e = 10^3$) that it does not allow line wing photons to thermalize to the continuum intensity level. Hence the far-wing line intensities fall significantly below the continuum level. First, we shall discuss the CRD results (curves 1 and 4). For the CRD mechanism, equations (25) and (26) reduce to

$$S(x, z) = \frac{(1-\varepsilon)}{2} \int_{-\infty}^{\infty} J(x', z)\, \phi(x')\, dx' + \varepsilon B \qquad (33)$$

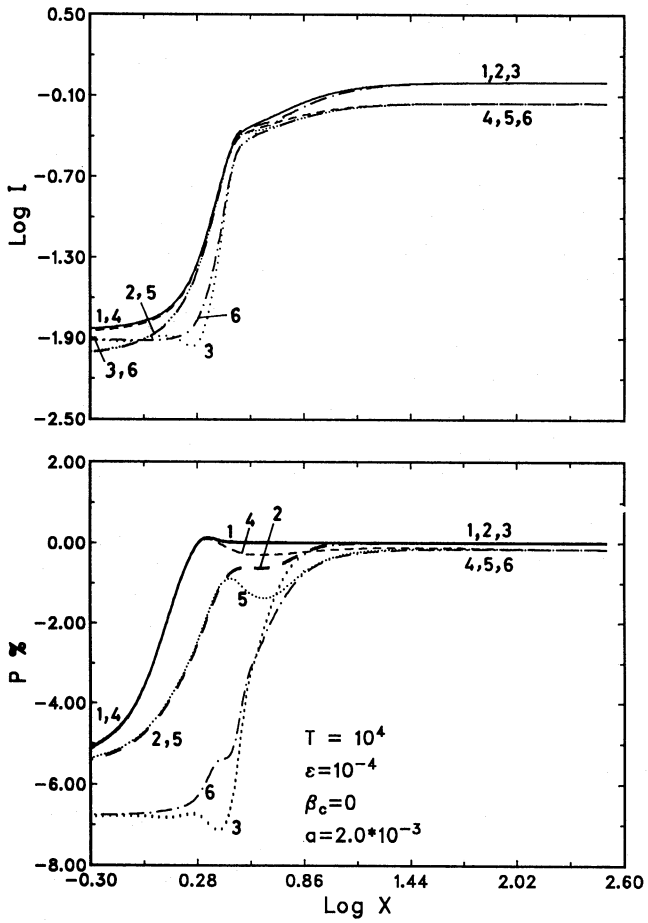

Figure 2. Same as Fig. 1, but for the optical thickness $T=10^4$. Also, in computing the results presented in this and subsequent figures, the medium is irradiated on the lower boundary with a frequency-independent isotropic radiation of unit intensity. Notice that the intensity profiles are in absorption, unlike the cases in Fig. 1.

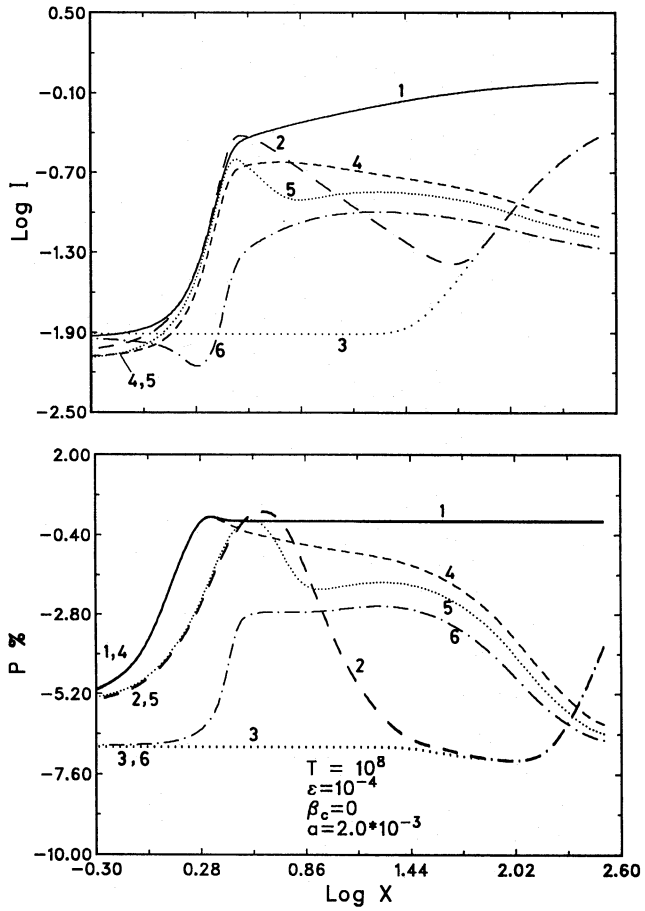

Figure 3. Same as Fig. 1, but for the optical thickness $T=10^8$, which gives results typical of lines formed in semi-infinite isothermal atmospheres.

and

$$P(x,z)=\frac{3(1-\varepsilon)}{16}\int_{-\infty}^{\infty}[J(x',z)-3K(x',z)]\,\phi(x')\,\mathrm{d}x'. \tag{34}$$

From equation (34), we see that the integrals give a frequency-independent polarization. One should bear in mind, however, that the contribution to the radiation field at different frequencies comes from different depth points (from the Eddington–Barbier relation), so that the frequency dependence of emergent polarization reflects a mapping of the anisotropy of the radiation field over depth. We see that PRD and CS show a higher percentage of polarization in the core than does CRD because the photons trapped by these mechanisms undergo a larger number of multiple scatterings, producing a higher percentage of polarization. Thermal sources denoted by the isotropic εB term are dominant over the scattering term in the source function for frequencies $x>100$, which reduces polarization. For an effectively thick medium, there is a considerable amount of NCES taking place in the wings (see curves 4, 5 and 6). Hence an electron-scattering polarization contribution seems to be superposed on the atomic CRD polarization profile. The polarization may reach a constant value only after several electron Doppler widths ($x\sim 500$–600) (compare also with the corresponding CRD polarization profile of Fig. 1).

The PRD profile without electron scattering (curve 2) has a deep absorption minimum in the wing of the intensity profile around $x=60$. The electron scattering seems to fill up this minimum completely, through a large number of scatterings of the line core photons into the line wing frequencies (curve 5). The polarization profile for PRD is characterized by a wide, deep negative polarization trough extending from $x=20$ to 120. The polarization gradually tends to zero in the very far wings ($x>320$). When non-coherent electron scattering is included, the magnitude of the negative polarization is reduced, and even

the frequency dependence is completely changed. The polarization is still unsaturated at $x \sim 300$, and it may saturate to a constant value only after several more electron Doppler widths.

The constant intensity throughout the frequency region ($0 < x < 25$) for CS (see curve 3) indicates that the source function $S^I_{\rm tot}(x, \mu, z)$ remains constant over optical depth up to $\tau(x) \sim 3 \times 10^4$. Hence we get constant polarization in the above-mentioned frequency range. This is a typical behaviour of coherent scattering mechanisms in semi-infinite atmospheres (see Rees & Saliba 1982). The intensity profile formed under the combined influence of CS and NCES has a more interesting frequency dependence (curve 6). The profile looks very similar to the corresponding (PRD + NCES) intensity profile, in the frequency range ($10 < x < 320$). When electron scattering is involved, the polarization profile looks like a box profile in the frequency range ($2 < x < 40$). Thus we observe that, for media of high optical thickness, electron scattering gives a positive contribution to the polarization in combination with PRD and CS, and negative polarization in combination with CRD.

In the absence of electron-scattering redistribution, atomic coherent scattering leads to a situation where transfer takes place independently in each frequency point of the line without any frequency coupling. The polarization profiles clearly show that the PRD (partial non-coherence) mechanism produces intermediate values of polarization when compared to the CRD (complete non-coherence) and CS (complete coherence) mechanisms. Thus, at least for optically thick resonance lines, the 'frequency coherence' of the atomic scattering process is directly related to the 'local anisotropy of the radiation field', irrespective of the optical depth under consideration. Note that non-coherent electron scattering dominates the transfer in the far wings ($x > 100$); so much so that the individual identities of CRD, PRD and CS are completely lost, and all three mechanisms produce intensity and polarization profiles which are not qualitatively different from each other.

3.4 Effect of optical thickness on polarization in an electron-scattering atmosphere

In Fig. 4 we show the effect of the optical thickness T on the resonance lines formed under the combined influence of PRD and NCES. Curves 1, 2 and 3 represent results for $T = 10^2$, 10^4 and 10^8 respectively, when $\beta_e = 0$. Curves 4, 5 and 6 represent, respectively, the same cases when $\beta_e = 10^{-5}$. The profiles corresponding to $T = 10^2$ here are completely different from those shown in Fig. 1, because in this case we have imposed an input radiation incident on the lower boundary of the slab. As expected, the intensity profiles become deeper and wider as the optical thickness is increased, finally reaching a saturation in the core for semi-infinite-type atmospheres. When NCES is introduced, this trend is not altered for the case $T = 10^2$. However, for $T = 10^4$ and 10^8, the NCES produces profiles which are quite different, in the wings, from the pure PRD intensity profile. The wing self-reversal of the $T = 10^8$ case is filled and an absorption profile with broad shoulders is produced. A similar, even stronger, effect is observed for the linear polarization profile. The $T = 10^8$ case without NCES (curve 3) produces a deep, wide negative polarization feature in the far wings ($10 < x < 200$), which is so strong that any significant changes in it can be employed as a diagnostic in modelling the polarization in resonance lines. A comparison of curves 3 and 6 shows that NCES reduces the percentage of polarization at certain frequencies in the wing ($10 < x < 100$). This can be understood as follows. In this frequency range, the numerator of equation (32) remains constant with frequency, due to the nature of $R^e(x, x')$, and the denominator increases, due to an increase in the magnitude of the electron source function $S^e(x, z)$. This results in a reduction in the emergent linear polarization.

3.5 Comparison of lines formed under coherent and non-coherent electron-scattering mechanisms

In Fig. 5 we show lines formed under PRD in combination with different choices of the electron-scattering mechanisms. The electron-scattering mechanisms selected are CES and NCES (equations 17 and 18 respectively). The coherent electron scattering, which is conventionally employed in the literature, leads to results that are quite different from the NCES results. Obviously, the use of CES for calculations involving scattering by free electrons leads to interpretations that are quantitatively different from those derived from calculations where free-electron scattering is properly incorporated through NCES. The dashed curves give the results for CES with $\beta_e = 10^{-5}$, and the solid curves give the NCES result for the same parameters. We see that atomic PRD operates in the line core and that electron scattering is dominant in the wings in both cases; CES gives a higher intensity in the near wings ($0 < x < 6$) and a smaller intensity in the far wings than does the NCES mechanism. This is because CES does not allow any frequency diffusion from the core into the wings, being a frequency-independent mechanism, and gives constant polarization in the wing. For CES, the contribution to the integration in equation (27) comes from the single monochromatic frequency under consideration. For NCES, however, the $S^e(x, z)$ contains contributions from the entire frequency range. $S^e(x, z)$ is therefore higher in magnitude for NCES than for CES, which leads to a smaller degree of polarization for NCES in the frequency range ($6 < x < 320$) than for CES.

3.6 Effect of variation of atomic continuum absorption β_C when the electron scattering is non-coherent

The atomic continuum absorption is represented by the parameter β_C. It is usual practice to add the contribution β_C from the free electrons to the atomic continuum absorption directly. However, when electron scattering is considered as a non-coherent

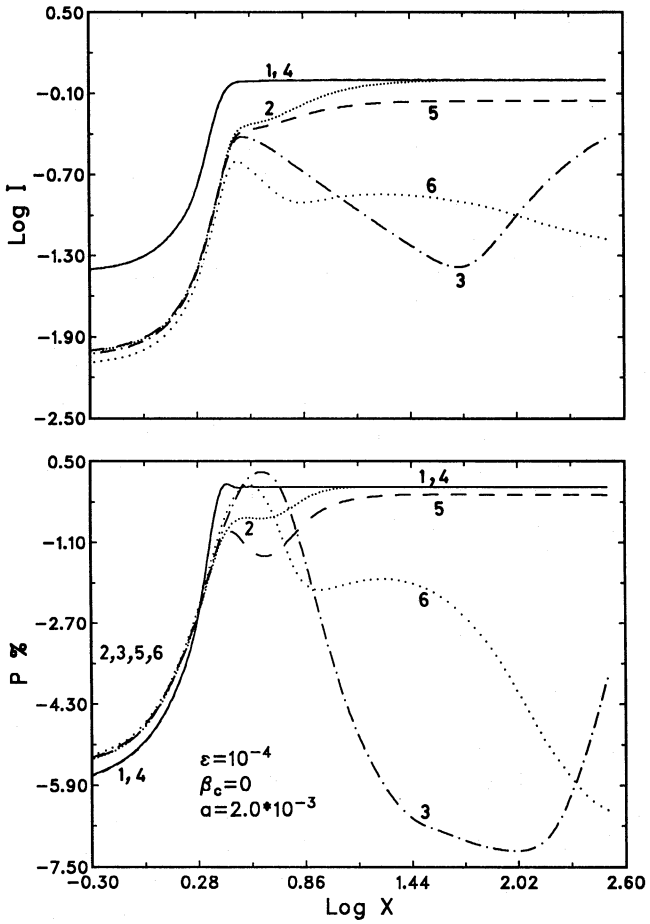

Figure 4. Effect of optical thickness T. Panels as in Fig. 1. Curves 1 (solid line), 2 (closely spaced dotted line) and 3 (dot-dashed line) represent the results for $T=10^2$, 10^4 and 10^8 respectively, when $\beta_e=0$. Curves 4 (short-dashed line), 5 (long-dashed line) and 6 (widely spaced dotted line) represent the corresponding cases when $\beta_e=10^{-5}$. The atomic line scattering mechanism employed is PRD. See also Figs 1–3.

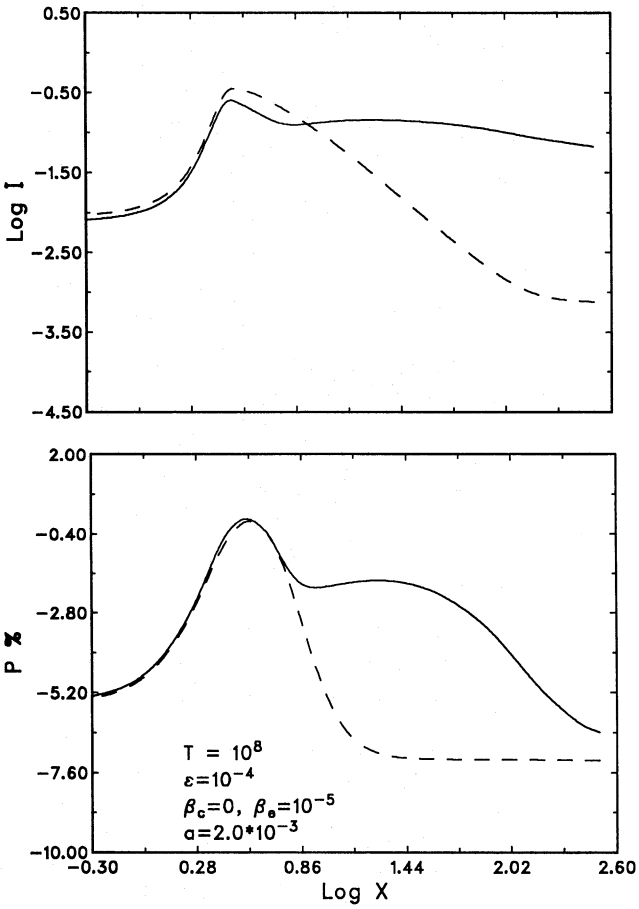

Figure 5. A comparison of the results for coherent electron scattering (CES, dashed lines) with non-coherent electron scattering (NCES, solid lines). Panels as in Fig. 1. The model parameters employed are shown in the lower panel. The atomic line scattering mechanism employed is PRD. Compare with corresponding $\beta_e=0$ case in Fig. 4.

mechanism, β_e is multiplied by a scattering integral involving the NCES function $R^e(x, x')$ (see equation 27). The effect of variation of β_C on moderately optically thick resonance line polarization is studied in Nagendra (1988) and the references quoted therein. In Fig. 6 we show the intensity and polarization profiles when β_C is varied in the range (0, 1). In all the cases discussed so far in this paper, we have chosen $\beta_C=0$. Faurobert (1988) has studied the effect of β_C for a semi-infinite medium (without including NCES). We have considered an optical depth $T=10^8$ that mimics (approximately) a semi-infinite medium. Our results, therefore, approximately match hers for a similar set of parameters (compare, for example, the $\beta_C=10^{-8}$ case, curve 3, with fig. 7 of the above-mentioned paper). Notice that variation of the continuum absorption drastically alters the wing polarization when $\beta_C<\beta_e$. We do not find the wing maximum mentioned in the above reference; this is essentially because of the introduction, here, of NCES. Larger values of the continuum absorption ($\beta_C \gg \beta_e$) make the spectral lines shallow and weak, as the lines reach continuum at frequencies closer to the line centre. The polarization, therefore, also tends to zero in the wings for the lines with $\beta_C \geq 10^{-3}$ (see curves 5 and 6). When $\beta_C=1$, an extremely weak line is formed. We can conclude that, generally, the larger the β_C, the smaller the percentage of polarization we obtain in the line wings.

3.7 Effect of variation of non-coherent electron scattering β_e on line formation

In Fig. 7 we show the intensity and polarization profiles when the parameter β_e is given variation in the range (0, 1). The parameter $\beta_e=0$ represents a case where electron scattering is ignored, and $\beta_e=1$ represents a case where it is as important as the averaged line centre absorption ($\chi^e=\chi^L$). There is no atomic continuum absorption in these models ($\beta_C=0$). When β_e is increased from 10^{-10} to 10^{-5}, the intensity increases in a frequency band ($10<x<100$), and the polarization correspondingly

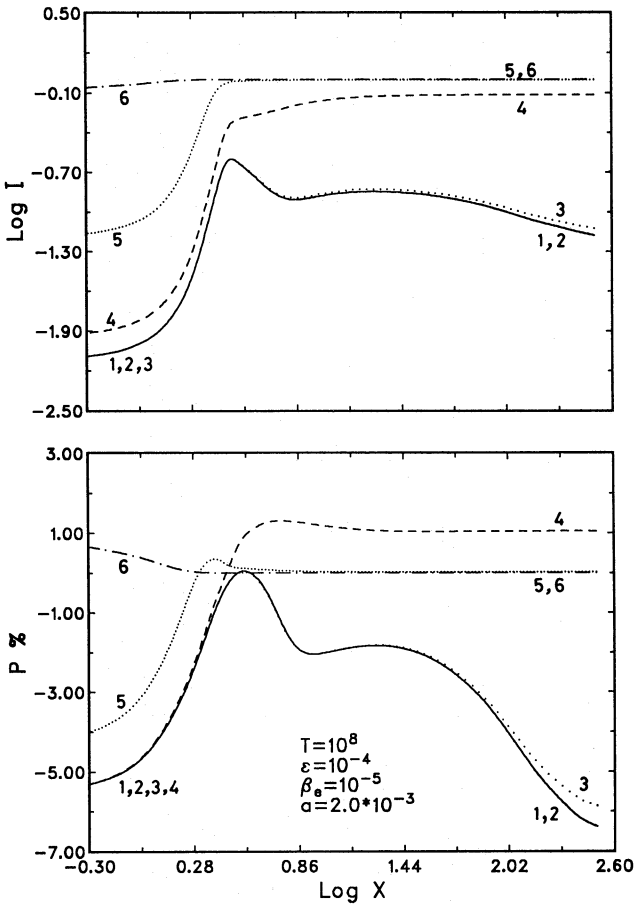

Figure 6. Effect of the continuum absorption parameter β_C. Panels and lines as in Fig. 1. Curves 1, 2, 3, 4, 5 and 6 represent $\beta_C = 0$, 10^{-10}, 10^{-8}, 10^{-5}, 10^{-3} and 1 respectively. A combination of atomic PRD with NCES is employed for line scattering. Other model parameters are shown in the lower panel.

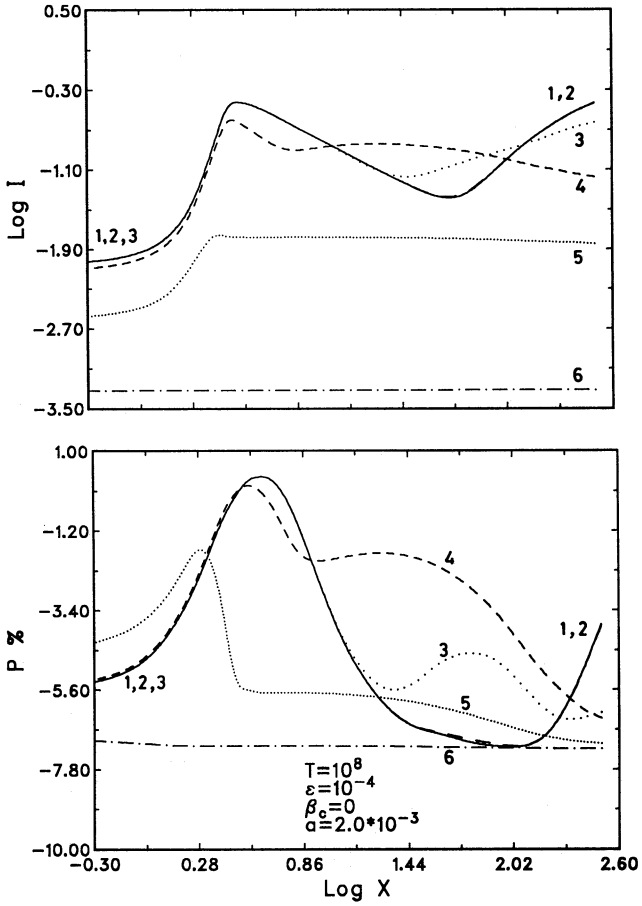

Figure 7. Effect of the electron scattering parameter β_e. Panels and lines as in Fig. 1. Curves 1, 2, 3, 4, 5 and 6 represent $\beta_e = 0$, 10^{-10}, 10^{-8}, 10^{-5}, 10^{-3} and 1, respectively, following the same convention employed in Fig. 6. A combination of PRD and NCES is used in the computations. See also Fig. 6.

decreases. For this range of β_e values, atomic line scattering still dominates over electron scattering in the wings. However, as β_e is increased further from 10^{-5} to 1, the intensity absorption profiles become more and more weak and narrow, and polarization increases until, for $\beta_e = 1$, the line intensity and polarization have insignificant variation across the profile. Due to the complete dominance of non-coherent electron scattering as β_e approaches 1.0, the line intensity itself becomes orders of magnitude smaller than standard model intensity profiles, since the line core and near-wing photons are redistributed over a very wide frequency band comprising several hundred Doppler widths. It can be seen, in contrast with Fig. 6, that, since $\beta_e = 1$ represents the largest amount of electron scattering, the polarization remains constant, but at the highest level across the line profile; unlike in the case of Fig. 6 (curve 6), where the polarization remains constant at the lowest level.

3.8 Effect of variation of thermalization parameter ε when the electron scattering is non-coherent

In order to show the effect of variation of ε on resonance lines, when non-coherent electron scattering is operating, we present profiles computed for ε values in the range (0, 1) in Fig. 8. When $\varepsilon = 0$, the line is purely scattering, with no contribution from local thermal sources to the line source function. At the other extreme, $\varepsilon = 1$ represents the LTE condition, where the only scattering mechanism, in the present situation, remains the electron scattering. The atomic scattering dominated lines ($\varepsilon \ll 1$) are in absorption, and the polarization profiles are predominantly negative. The atomic contribution to the emergent polarization is relatively strong compared to the NCES contribution, except in the far wings. As the parameter $\varepsilon \to 1$, the emergent intensity profile becomes an emission profile, the atomic contribution to the line polarization approaches zero, and only the NCES contribution remains, affecting the line polarization in the characteristic manner discussed earlier. Also, the negative polarization decreases across the line core region.

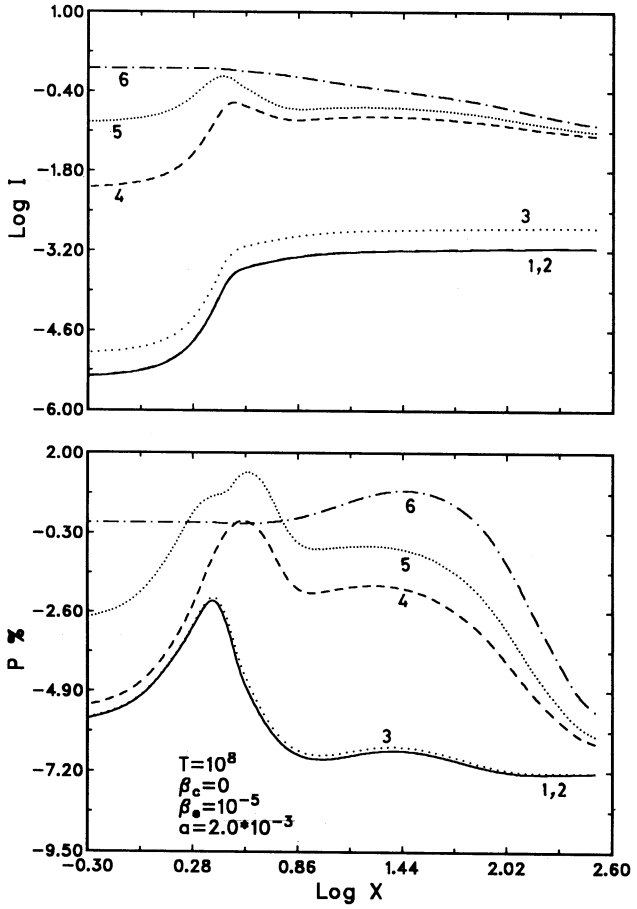

Figure 8. Effect of the thermalization parameter ε. Panels and lines as in Fig. 1. Following the same convention as employed in Fig. 6, curves 1, 2, 3, 4, 5 and 6 represent $\varepsilon = 0$, 10^{-10}, 10^{-8}, 10^{-4}, 10^{-2} and 1. A combination of PRD and NCES is used in the computations. See also Figs 6 and 7.

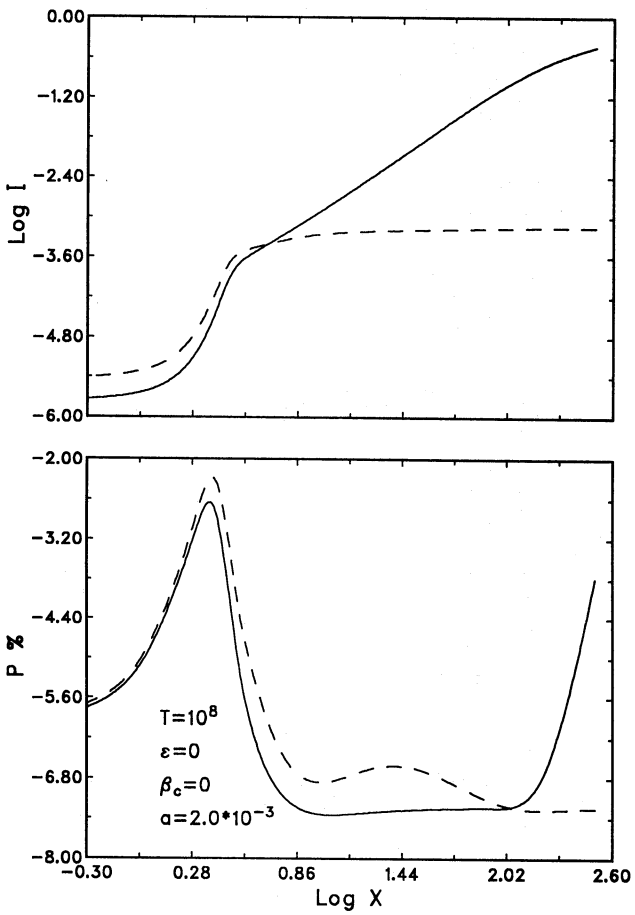

Figure 9. Effect of electron scattering in a conservative scattering atmosphere ($\varepsilon = \beta_C = 0$). The solid lines represent the case of no electron scattering ($\beta_e = 0$), and the dashed lines represent the case of NCES (with $\beta_e = 10^{-5}$). Panels as in Fig. 1. Other model parameters are shown in the lower panel. The atomic line scattering mechanism employed is PRD.

3.9 Effect of non-coherent electron scattering on lines formed in a conservative scattering atmosphere ($\varepsilon = \beta_C = 0$)

We discuss this aspect using Fig. 9. In a conservative scattering medium ($\varepsilon = \beta_C = 0$), the line is perfectly scattering, with no contribution from thermal radiation. When there is no electron scattering ($\beta_e = 0$, solid curves), the line core is deeper than for the non-conservative cases discussed in previous sections, and the intensity profile rapidly approaches the level of the incident radiation intensity [$I(x, \mu, \tau = T) = 1$] in the far wings ($x > 150$). The contribution to $S^Q_{\rm tot}(x, \mu, z)$ in this frequency range comes from deep within the atmosphere, where anisotropy is small. Emergent polarization therefore also reduces gradually to zero level in this frequency range. When NCES is included ($\beta_e = 10^{-5}$, the dashed curves), it effectively enhances the line core intensity and produces flat and broad lower intensity wings. We find that PRD with NCES gives lower polarization in the frequency range ($2 < x < 100$) than does PRD without NCES. This and the constancy of polarization beyond $x = 100$ are essentially due to the introduction of the $S^e(x, z)$ term in $S^I_{\rm tot}(x, \mu, z)$, as already pointed out.

4 CONCLUSIONS

In this paper we have indicated, through detailed illustration, that electron scattering, being an important source of opacity in early-type stellar atmospheres, deserves correct treatment when it is included in line formation problems aimed at modelling the observed linear polarization in resonance line profiles. It is sufficient to incorporate non-coherent electron scattering (NCES) in a similar way to that presented here, namely as an additional redistribution mechanism in a two-level atom source function. The effectively thin ($\varepsilon T \ll 1$) and effectively thick ($\varepsilon T \gg 1$) spectral lines show measurable changes of the emergent polarization in the wings due to the NCES mechanism. This result may be important for diagnosis purposes. It is clearly seen that free-electron redistribution produces changes in intensity and polarization in a manner that is rather characteristic of that mechanism. Hence

the correct modelling of wing polarization, in particular that of resonance lines, requires inclusion of NCES in the diagnostic computations.

ACKNOWLEDGMENTS

One of us (KNN) would like to thank Dr H. Frisch for providing a copy of the code for computation of the redistribution function $R_{\mathrm{II-A}}(x, x')$ by Adam's method. We would also like to thank Professor A. Peraiah for his constant encouragement. We are grateful to Mr B. A. Varghese for his help in making the figures shown in this paper.

REFERENCES

Adams J. F., Hummer D. G., Rybicki G. B., 1971, J. Quant. Spectrosc. Radiat. Transfer, 11, 1365
Auer L. M., Mihalas D., 1968, ApJ, 153, 245
Chandrasekhar S., 1950, Radiative Transfer. Oxford Univ. Press, Oxford
Faurobert M., 1987, A&A, 178, 269
Faurobert M., 1988, A&A, 194, 268
Hillier D. J., 1991, A&A, 247, 455
Hubeny I., 1985, A&A, 145, 461
Hummer D. J., 1962, MNRAS, 125, 21
Hummer D. J., 1969, MNRAS, 145, 95
Mihalas D., 1978, Stellar Atmospheres. Freeman, San Francisco
Nagendra K. N., 1988, ApJ, 335, 269
Rangarajan K. E., Mohan Rao D., Peraiah A., 1991, MNRAS, 250, 633
Rees D. E., 1978, PASJ, 30, 455
Rees D. E., Saliba G., 1982, A&A, 115, 1